



Full Length Article

Environmental waste-derived dual heteroatom-rich sustainable carbon as anodes for Li- and Na-ion batteries

Ramkumar Balasubramaniam^a, Ranjith Thangavel^{b,c}, Hariharan Dhanasekaran^a,
Megala Moorthy^a, Sangho Park^d, Werayut Srituravanich^e, Hyun-Yong Lee^{a,*}, Yun-Sung Lee^{a,*}

^a Faculty of Chemical Engineering, Chonnam National University, Gwangju 500757, Republic of Korea

^b School of Energy Science and Engineering, Indian Institute of Technology Guwahati, Guwahati 781039, India

^c Department of Chemical Engineering, Indian Institute of Technology Tirupati, Tirupati 517619, India

^d School of Chemical Engineering, Jeonbuk National University, Jeonju 554896, Republic of Korea

^e Department of Mechanical Engineering, Faculty of Engineering, Chulalongkorn University, Bangkok 10330, Thailand

A B S T R A C T

In this study, we demonstrate the use of dual heteroatom-doped (i.e., N- and S-doped) porous carbon derived from the filters in cigarette butts, which are categorized as solid environmental waste. We use a facile, sustainable, and inexpensive method and green chemical activation for application in LIBs and SIBs. The carbon prepared by activating melamine is highly porous with rich and mesopores along with a high Brunauer-Emmett-Teller (BET) surface area ($815.8 \text{ m}^2 \text{ g}^{-1}$) and pore volume ($0.404 \text{ cm}^3 \text{ g}^{-1}$). The favorable textural properties, such as enlarged interlayer d-spacing, edge defects, electrochemically active N and S functionalities, and high electronic conductivity, make this porous carbon an attractive candidate for both Li- and Na-ion storage applications. The porous carbon delivered high capacities of $\sim 872 \text{ mAh g}^{-1}$ and 289 mAh g^{-1} at 500 mA g^{-1} when employed as anodes for LIBs and SIBs, respectively. The high-performance porous carbon materials developed via the proposed green and sustainable approach can be applied to advanced energy storage systems.

Introduction

Over the past few decades, rechargeable Li-ion batteries (LIBs) have received global attention in relation to several portable applications such as electronic devices and electric vehicles owing to the high energy density, long cycle life, low self-discharge rate, and no memory effect of these LIBs [1–15]. The energy–density demand for next-generation applications cannot be satisfied by commercial LIBs due to the theoretical capacity limitations of electrode materials. In particular, graphite, the first commercialized anode material, which is still used in state-of-the-art LIBs, exhibits a specific capacity of $\sim 372 \text{ mAh g}^{-1}$ [16]. Unfortunately, the low intrinsic capacity, rate capacity, and safety concerns owing to Li-plating and Li-dendrite formation have limited the usage of graphite anodes in LIBs [17,18].

Moreover, Na-ion batteries (SIBs) have received considerable attention due to low cost, abundant availability, and similar storage mechanism to that of LIBs. SIBs are considered to be the most promising energy storage devices for large-scale energy storage systems [19,20]. The larger ionic radius (1.02 \AA) of an Na ion than that of an Li-ion (0.76 \AA) impedes the facile Na-ion insertion and extraction potentials in various electrode materials used in LIBs, limiting the availability of hosts for

SIBs, thereby preventing the development of SIB technology [21,22]. Although graphite anodes were commercialized for use in LIBs, these anodes do not support Na^+ -ion intercalation, and several amorphous and disordered carbon materials such as hard carbon, carbon sheets, graphene, and nanostructured carbon have been studied as anode materials for SIBs. However, hard carbon has disadvantages such as high hygroscopicity, low density ($1.5\text{--}1.8 \text{ g cm}^{-3}$), capacity degradation at higher current densities, and the possibility of Li-metal deposition during the charging process [23]. Unlike those of bulk materials, the synthesis procedures of nanomaterials are expensive and require complex operations. Additionally, the procedures have low productivity, the products have low purity, and controlling grain sizes is difficult [17].

To promote the practical usage of high-energy–density LIBs and SIBs, high-capacity anode materials must be explored. Several transition metal oxides, metals, alloys, metal sulfides and phosphides, and conductive polymer-based anode materials have been studied as anode materials [9,10,19,24–28]. Although these anode materials demonstrate high capacity, they exhibited poor cycle life owing to large volume expansion during lithiation and sodiation. Additionally, alloy anode materials exhibit low electronic conductivity and large volume changes during the charge and discharge processes [17].

* Corresponding authors.

E-mail addresses: hyleee@jnu.ac.kr (H.-Y. Lee), leeys@chonnam.ac.kr (Y.-S. Lee).

<https://doi.org/10.1016/j.jiec.2024.12.036>

Received 10 July 2024; Received in revised form 12 December 2024; Accepted 19 December 2024

Available online 25 December 2024

1226-086X/© 2024 The Korean Society of Industrial and Engineering Chemistry. Published by Elsevier B.V. All rights are reserved, including those for text and data mining, AI training, and similar technologies.

Different types of domestic, industrial, and agricultural waste have emerged as attractive sources of porous carbon for application in energy storage devices. The architecture of waste-derived porous carbon can be tailored and has a high surface area along with a large pore volume. Additionally, these carbon materials can be mesoporous and their surface chemistry can be tuned. The favorable structural and textural properties of waste-derived carbon can yield several active sites for Li- and Na-ion storage, thereby yielding high-energy-density LIBs and SIBs. Waste-derived porous carbon-based materials have garnered considerable attention owing to their cost-effectiveness, structural stability, reasonable capacity, versatility, and availability [28,29,30]. Recently, several studies have been conducted on the synthesis of carbon from several waste materials such as coffee oil, fruit, and grounds [10,29,31,22,32–34]. For instance, Kim et al. reported that spheroidal carbon particles obtained from coffee oil could be used for Li-, Na-, and K-ion storage; [29] Blankenship et al. reported cigarette butt-derived carbons for achieving high hydrogen storage capacity; [34] Yu et al. reported the fabrication of LIBs using an N-doped carbon anode prepared using cigarette butts [33]. However, studies on carbon derived from cigarette butts as anode materials for SIBs are limited.

The production of porous carbon via green and sustainable approaches is crucial for ensuring the sustainability of waste-derived porous carbon. The conventional pore-activation technique involves physical activation through steam or CO₂ at a high temperature of 1200 °C. In particular, the most common method for producing porous carbons from waste materials involves chemical activation using KOH, H₃PO₄, ZnCl₂, Na₂CO₃, and KHCO₃ to yield highly porous architectures. However, KOH, which is most commonly used, is highly corrosive, and H₃PO₄ and ZnCl₂ are toxic activating agents that are considered to be “high risk.” [35] Moreover, several environmental risks associated with conventional chemical activating agents demand the development of green chemical activation methodologies for porous carbon. Herein, we study the development of sustainable porous carbon from waste cigarette butts through the chemical activation of melamine as a green chemical agent.

Clean and waste-management-based energy storage and conversion technologies are increasing in importance for the future development of sustainable energy storage materials. Waste management is anticipated to become a major opportunity in the future. Cigarette butts are an underrated pollutant and have affected the ecosystems at several locations. Cigarette butts contain cigarette filters, which are currently an environmental pollutant because these filters are non-biodegradable [34]. A cellulose derivative is the principal component of cigarette filters [34,36]. The annual worldwide cigarette consumption is 5.8 trillion and generates 8,00,000 metric tons of cigarette butts, [34,36] which contain toxic elements and cause harm to humans and wildlife. The environmentally hazardous cigarette butts can be used as a source of active carbon for electrode materials. Additionally, N-enriched melamine activation is used to prepare mesoporous N-doped carbon [37].

Moreover, surface-chemistry modifications of porous carbon by introducing heteroatom dopants are a versatile approach for improving Li- and Na-ion storage performances. Heteroatom doping with N, S, P, and B was proposed as an effective approach for increasing the Li- and Na-ion storage in several porous carbon materials [28,38–43]. Recently, the dual-heteroatom-doping strategy applied to carbon frameworks yielded superior performances during electrocatalysis but has not been widely investigated for high-energy battery applications [44,45]. Additionally, we investigated the effects of doping N and S heteroatoms in sustainable porous carbon derived from cigarette butts on Li- and Na-ion storage performances. S dopants with a large ionic size (1.04 Å) can increase interstitial distances, capacities, and power capabilities of anode materials [39,46,47]. Furthermore, N dopants generate additional Na-storage sites and electrons, as well as increase the carrier concentration, electrical conductivity, and the ion storage capacity, of the carbon material [39,40]. The present study developed a dual heteroatom-doped (N- and S-doped) porous carbon (NSC) derived from

cigarette butts via a melamine-assisted sustainable approach for use as anode materials for LIBs and SIBs. The porous carbon obtained via melamine activation exhibited highly favorable textural properties, i.e., a high Brunauer-Emmett-Teller (BET) surface area (815.8 m² g^{−1}) and pore volumes (0.404 cm³ g^{−1}). The porous carbon delivered a high capacity of ~619 mAh g^{−1} and 119 mAh g^{−1} at 500 mA g^{−1} when employed as an anode for LIBs and SIBs, respectively. The ion storage kinetics of the waste-derived carbon were greatly enhanced by the synergistic benefits of N and S heteroatoms for delivering remarkable rate performances (872 mAh g^{−1} and 289 mAh g^{−1} at 500 mA g^{−1}) along with excellent cycle performances (>1000 cycles), outperforming conventional carbon anodes. The results of the study will enable the emergence of inexpensive next-generation energy storage devices for practical applications.

Experimental Section

Preparation of N and S-doped carbon

Cigarette butts were used to prepare the NSCs. The wrapping paper was first removed from the filter to avoid reaction and contamination. Next, the filters were heated at 250 °C for 5 h at a heating rate 5 °C/min in a beaker. The resulting powder was mixed with melamine (10 wt%) in water at 100 °C. After drying the precursor, it was transferred to a tubular furnace for heating at 500 °C for 2 h in an N₂ atmosphere (heating rate 1 °C/min). The resulting powder was pulverized in a high-energy ball milling machine for 12 h. Subsequently, the powder was placed in a tubular furnace and heated at 800 °C for 2 h in an N₂ atmosphere at a heating rate of 2 °C/min. Subsequently, the powder was ground with S in a 1:1 ratio and heated at 500 °C for 2 h in N₂ atmosphere. The resulting powder was denoted as NSC for further studies. Cigarette filter/butt-derived carbon (CC) was prepared using the same method without N and S doping. Furthermore, the precursor carbon (PC) was prepared by same procedure without doping and heat temperature treatment at 250 °C for 5 h. That powder called as precursor carbon (PC). The resulting powder was used for further physio-chemical and electrochemical studies.

Material characterizations

The crystal structure of the prepared carbon was investigated using high-resolution X-ray diffraction (HR-XRD) (D/MAX Ultima III, Japan). The morphology and elemental distributions of the synthesized carbon was investigated using field-emission scanning electron microscopy (FE-SEM) and energy dispersive X-ray analysis (Hitachi, Japan, S-4700/EX-200) and high-resolution transmission electron microscopy (HR-TEM) (JEM-2000, EX-II, JEOL, Japan). Raman spectra were recorded on a LabRam HR800 UV Raman microscope (Horiba Jobin-Yvon, France: excitation wavelength of 515 nm). Surface area and pore size distribution were analyzed using a surface area analyzer (Belsorp mini II, BEL, Japan). The surface components of the sample were investigated using X-ray photoelectron spectroscopy (XPS) (multiLab2000 XPS (ESCA), VG, UK).

Electrochemical measurements

Electrode slurries were prepared by using 70 wt% of the active material, 20 wt% of Super-P, and 10 wt% of polyvinylidene fluoride in an N-methyl-2-pyrrolidone solvent. The prepared slurries were casted onto the surface of a Cu current collector using the doctor blade method. The cast slurry was heated at 80 °C overnight to remove the solvent. After drying, the electrodes were cut into 1.4-cm circular disks and assembled into a 2032-coin cell for investigating electrochemical performance. The loading mass of the electrode was 1.5–2 mg cm^{−2}. Then, Li metal foil was used as a counter and reference electrode, and 1 M LiPF₆ [1:1 EC/DMC (Ethylene Carbonate/Dimethyl Carbonate) solvent] was used as a

electrolyte with a Celgard polypropylene separator and glass fiber. The Na-ion battery was assembled using Na metal as a counter and reference electrode, and 1 M NaClO₄ (EC solvent) was used as an electrolyte with glass fiber as a separator. Electrochemical impedance spectroscopy (EIS) and cyclic voltammetry (CV) were conducted on the 2032-coin cell (Biologic, VSP, France) in the potential range of 0.01–3 V vs Li/Li⁺ and 0.01–3 V vs Na/Na⁺. The galvanostatic charge–discharge performance of the cell was tested at the same potential window range using BTS-2000 at 25 °C. For high loading mass, the electrode was prepared by using a gum electrode method. The Gum Electrodes were prepared using 20 mg of the active material, 3 mg of Ketjen black, and 2 mg of TAB binder in an ethanol solvent. Furthermore, the gum electrode was heated at 160 °C for 4 h to remove the solvent. Then, 1.4-cm circular disks are used as a cathode current collector. Same method is used to

prepare the NaCrO₂ gum electrode. In CSN//NaCrO₂ full-cell studies, prior to testing, the carbon anode was pre-sodiated for a few hours to improve charge storage performance. The cell was tested in the voltage range of 2–3.6 V, and the N/P ratio for the full cell was maintained at 1:1.6.

Results and discussion

Physiochemical characterization

Fig. S1 exhibits the XRD patterns of the precursor of carbon (PC), CC, and NSC samples. The diffraction patterns distinctly show two broad peaks corresponding to the (002) and (100) planes, representing the amorphous and crystalline natures of the CC and NSC materials. The

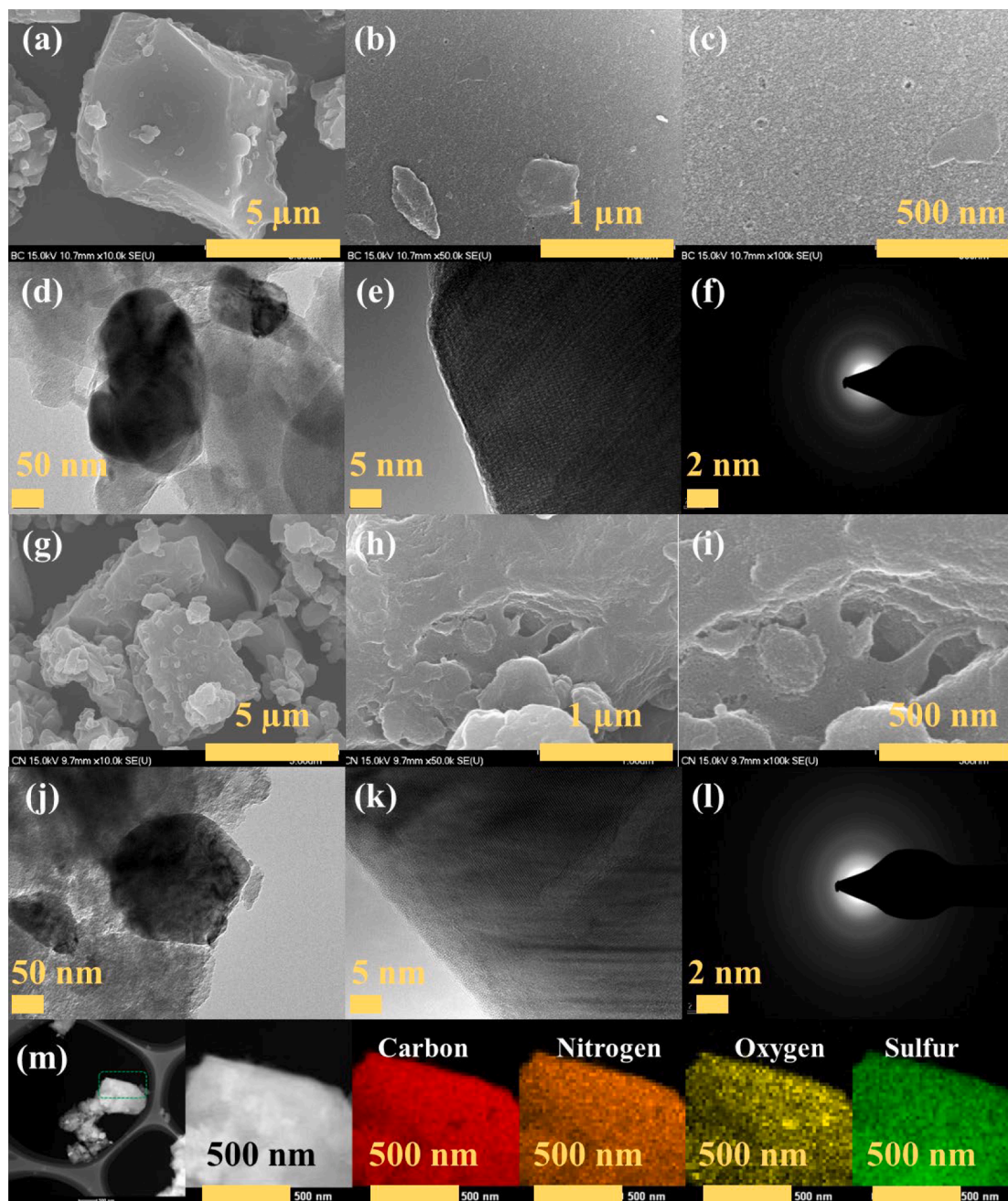


Fig. 1. Field-emission scanning electron microscope images of the (a, b, and c) cigarette filter/butt-derived carbon (CC) and (g, h, and i) N, S-doped porous carbon (NSC). Transmission electron microscope (TEM) and high-resolution TEM images of the (d, e) prepared carbon and (j, k) NSC. Selected area electron diffraction patterns of (f) CC and (l) NSC. (m) Energy dispersive spectroscopy maps of the NSC particles.

(002) diffraction peak obtained from the NSC sample was located at approximately 23.5° , which is much less than that of the CC sample (25.2°). Based on Bragg's equation ($n\lambda = 2d\sin\theta$), the interlayer spacing of NSC is 3.78 \AA , significantly higher than that of the CC sample (3.53 \AA), indicating that the prepared NSC can be favorable for storing large Na^+ ions. These outcomes confirm that the presence of N and S heteroatoms in the carbon framework expanded the interlayer spacing of disordered carbon [41,48].

Surface morphology analysis

The morphologies of the as-prepared CC and NSC samples were characterized by FE-SEM analysis. Fig. 1a–c and g–i reveal that the CC and NSC particles possess coarse morphologies. The average sizes of the particles were in the range of $2.3 \text{ }\mu\text{m}$. Both CC and NSC samples displayed more of a mesoporous nature (Fig. 1c and 1i). During the carbonization process, self-assembled melamine formed mesopores on the surfaces of the NSC particles. At a high temperature, the decomposed melamine products reacted with carbon atoms to dope N atoms in NSC and instantaneously increased the pores by etching. The mesoporous nature of CC and NSC were further examined via TEM and HRTEM analyses. In Fig. 1d, e, j, and k, no obvious long-range order is observed, signifying that CC and NSC have amorphous structures. The selected area electron diffraction patterns (Fig. 1f and l) of CC and NSC displayed

diffused rings, which further confirmed the amorphous characteristics of the materials (Fig. 1m, Fig. S2, and S3). The elemental and line maps obtained from energy dispersive spectroscopy conducted on the NSC particles indicate the homogeneous distribution of C, N, and S throughout the particle.

N_2 adsorption–desorption tests were conducted to investigate the porosities of the CC and NSC samples. Fig. 2a reveals that the two prepared samples exhibit properties of type I isotherms combined with type IV isotherms, which indicates the presence of mesopores. The BET specific surface areas of CC and NSC were $490.58 \text{ m}^2 \text{ g}^{-1}$ and $815.8 \text{ m}^2 \text{ g}^{-1}$, respectively. N and S doping increased the BET specific surface area of NSC with respect to that of CC. In this study, melamine in hot water is self-assembled with the carbon precursor to obtain a high-N-content precursor in a cold environment [37]. During carbonization, the decomposition products of melamine reacted with carbon atoms to dope the carbon framework with N and S. These distributions are primarily located at 2.44, 3.32, and 3.76 nm , confirming the presence simultaneously enlarge the pores by etching [49]. Further, S doping generated defects and pores and enlarged interlayer distances [50]. The pore-size distributions of CC and NSC are shown in Fig. S4. of mesopores in the prepared samples. Especially, the porous structure and high surface area of the acquired NSC can reduce the Li^+ and Na^+ diffusion lengths at the electrode–electrolyte interface and increase the Li^+ and Na^+ insertion and extraction capabilities, thereby decreasing internal resistance and

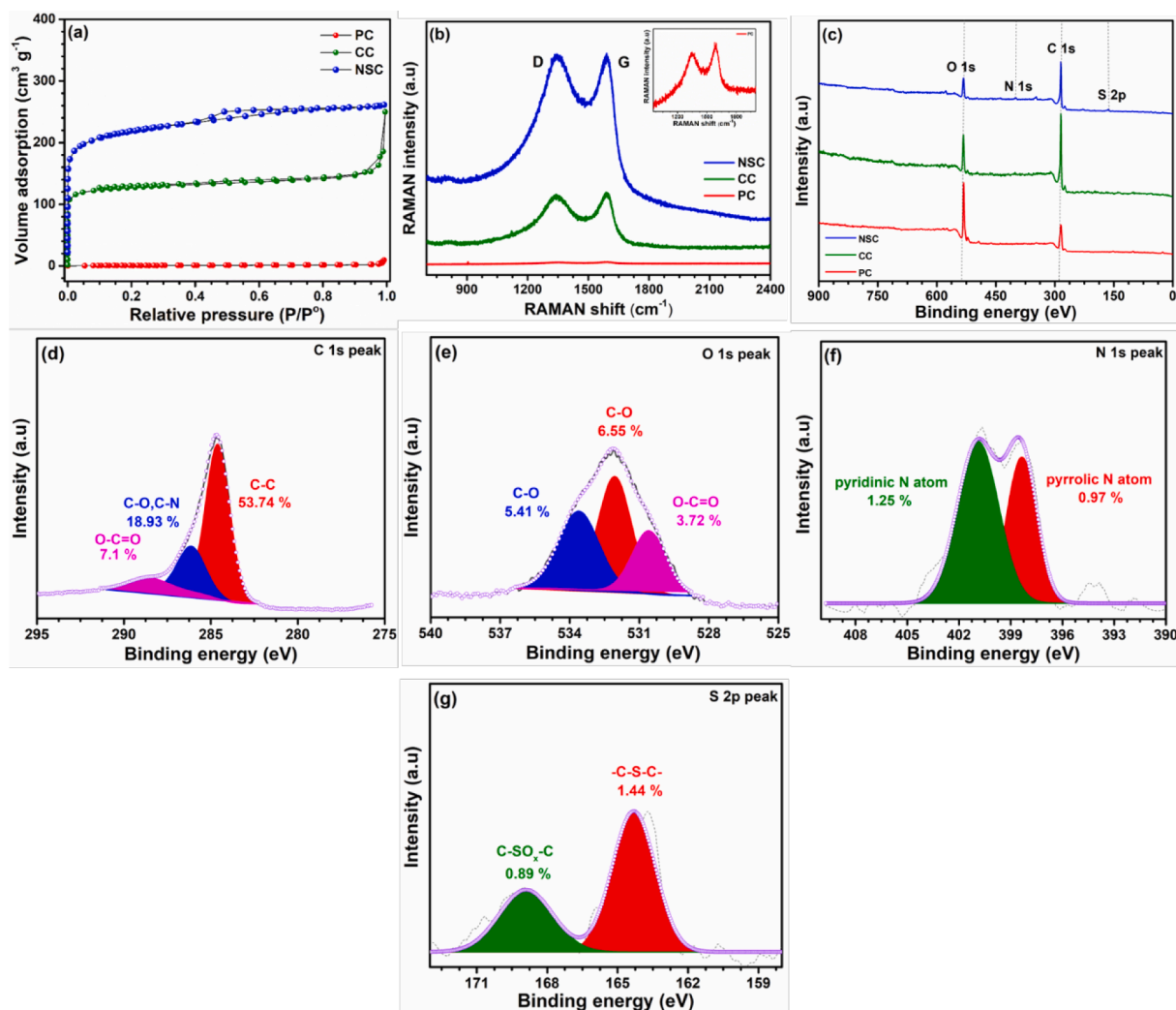


Fig. 2. (a, b, c) N_2 adsorption/desorption isotherms, Raman and full-range X-ray photoelectron spectra of the precursor of carbon, cigarette filter/butt-derived carbon, and N and S-doped porous carbon. (d) C 1s, (e) O 1s, (f) N 1s, and (g) S 2p spectra obtained from NSC.

ensuring high rate capabilities [41,47].

The Raman spectra of CC and NSC (Fig. 2b) display a characteristic D band with sp^3 hybridization at 1340 cm^{-1} and a G band with sp^2 hybridization at 1590 cm^{-1} [51,52]. The relative intensity ratio (I_D/I_G) of the D and G bands can be used to calculate the disordered degree of prepared carbon materials. Compared with that of the CC sample (0.959), the disordered degree of the NSC sample was higher (0.993), indicating a reduction in the average size of the sp^2 domain and the increase in the disordered structure owing to defects on the edge sites after N and S doping. Compared with the improving the Na^+ adsorption sites [41,47]. The increase in edge defects can increase ion storage perfect sites, the doping-induced defect sites have lower Na^+ adsorption energy, which is favorable for in porous carbon via pseudocapacitive storage.

XPS was further conducted to observe the chemical states of CC and NSC (Fig. 2c and Fig. S5). As presented in Fig. 2c, four main peaks are located at 284.6, 531.33, 399.58, and 163.9 eV, which correspond to C 1s, O 1s, N 1s, and S 2p, respectively.[41] Here, C 1s was deconvoluted into three peaks representing different functional groups. The peaks at 284.63, 285.98, and 287.56 eV correspond to sp^2 hybridized C–C, C–N/C–O, and O=C–O groups, respectively (Fig. 2d).[53,54,55] The N 1s spectrum was deconvoluted into two components, i.e., pyrrolic N at 400.53 eV and pyridinic N at 397.75 eV (Fig. 2f).[56,57,58] N doping can generate extrinsic defects and control the intrinsic electronic state of adjacent carbon, thereby improving electric conductivity and chemical activity.[47] Additionally, the S 2p spectrum of NSC was located at 164.32 eV, corresponding to the –C–S–C– bond.[21,42,58] The additional peak at 168.9 eV can be indexed as the C–SO_x–C group (Fig. 2g). [41,42] These results confirmed that N and S were successfully doped into the NSC structure. The XPS elementary analysis confirmed that the N and S contents in NSC were approximately 1.4 and 1.75 wt%, respectively. Several dual heteroatoms in the porous carbon framework can provide several active sites for ion storage via adsorption. Additionally, the conductivity and surface wettability of the electrode by the electrolyte increase owing to the presence of dual heteroatoms, which is favorable for high-capacity ion storage at high current rates.

Cyclic voltammetry

A 2032-type coin cell was used to analyze the electrochemical behavior of CC and NSC in terms of Li- and Na-ion insertion and extraction in the CC and NSC. The CV curves of the CC and NSC samples for the first three cycles measured in the potential range of 0.01–3 V vs Li/Li⁺ and Na/Na⁺ at a scan rate of 0.1 mV s^{-1} are presented in Figs. S6 and S7. The NSC anode yielded an irreversible cathodic peak in the range of 0.4–1.2 V vs Na/Na⁺ in the first cycle; this peak disappeared in subsequent cycles, which can be attributed to the formation of the solid-electrolyte interphase (SEI) and decomposition of the electrolyte (Fig. S7b) [31,41]. The CV curve presented in Figs. S7a and b reveals that the NSC//Na and NSC//Li cells operate under a similar storage mechanism during the charge and discharge processes. At the low-voltage region, the CV curves of NSC display reversible reduction and oxidation peaks located at approximately 0 and 0.11 V, corresponding to Na^+ insertion and extraction in carbonaceous materials, respectively [31,41]. The shape of the CV curve was approximately rectangular over a potential range of 0.15–1.2 V, which represents the capacitive storage behavior of Na^+ ions [22,41]. The CV curves of CC are related to that of NSC, representing a similar mechanism for Na^+ storage (Fig. S7b).

Figs. S8, S9, and S10 show the cycling profiles during Li insertion and extraction in the PC, CC, and NSC electrodes at a 500 mA g^{-1} current density for selected cycles (Figs. S8a, S9a and S10a). The initial discharge capacity of NSC was 872 mAh g^{-1} , which is higher than those of the CC (619 mAh g^{-1}) and PC (758 mAh g^{-1}) anode. Additionally, the Coulombic efficiency of NSC (63 %) was higher than that of the CC (23.1 %) and PC (15.9 %) anodes. The high discharge capacity and the moderate charge capacity of the NSC electrode led to the formation of the SEI

layer, electrolyte decomposition, and Li-ion irreversibility [1,59]. The high Coulombic efficiency of NSC is attributed to the reduced numbers of oxygen functional groups on the surface of NSC after N and S doping. The dual heteroatoms eventually improved electronic conductivity, thereby enhancing Li-ion storage capability by providing additional active sites. In the following cycles, the Coulombic efficiency of the NSC cell reached $\sim 99\%$, and the incomplete stabilization of the SEI layer was the main cause of irreversible capacity loss during each cycle [1,59]. After 1000 cycles, the reversible capacity (379 mAh g^{-1}) of NSC was considerably higher than that of CC (Fig. S10b). Overall, the NSC electrode offered higher capacity, Coulombic efficiency, and retention rate than the CC electrode, which can be attributed to the following properties: (i) enlarged interstitial distance and (ii) high specific surface area.

In addition, to understand the electrochemical characteristics of CC and NSC, the rate capabilities of these electrodes were examined in the range of $50\text{--}1000\text{ mA g}^{-1}$. Fig. S9c reveals that the CC electrode provides discharge capacities of 1061, 419, 364, 302, and 256 mAh g^{-1} while cycling at 50, 100, 200, 500, and 1000 mA g^{-1} , respectively. The cell retained a discharge capacity of 368 mAh g^{-1} , whereas the current density returned to 50 mA g^{-1} . In contrast, the NSC electrode provided improved discharge capacities of 1081, 575, 490, 403, and 334 mAh g^{-1} at the same current densities (Fig. S10c). Subsequently, the NSC electrode recovered the capacity of 509 mAh g^{-1} when the current density returned to 50 mA g^{-1} (Fig. S10d). According to the aforementioned studies, the LIB electrochemical performances of NSC were enhanced considerably with respect to those of CC and the reported graphitic anode materials (theoretical capacity of $\sim 372\text{ mAh g}^{-1}$) [60]. The superior discharge capacity can mainly be attributed to the larger inter-layer spacing in NSC (3.78 \AA based on the XRD results) than that of the graphite anode (3.34 \AA). Additionally, the increased discharge capacity and rate capability can be attributed to N and S doping, yielding additional storage sites as well as high interstitial distance and surface area.

Galvanostatic charge–discharge performance of the NSC//Na cell

Performance of the Na-ion battery

Fig. S8, S11, and Fig. 3 illustrate the charge and discharge profiles of PC, CC, and NSC vs Na/Na⁺ at a current density of 500 mA g^{-1} . The initial discharge and charge capacities of the PC anode were 223 and 58 mAh g^{-1} , respectively, with a Coulombic efficiency of 26 % (Fig. S8c). The CC anode provided initial discharge and charge capacities of 296 and 119 mAh g^{-1} , respectively, with a Coulombic efficiency of 40.2 % (Fig. S11a). In contrast to the PC and CC anodes, the NSC anode-based SIB exhibited first discharge and charge capacities of 520 and 289 mAh g^{-1} , respectively, and a corresponding initial Coulombic efficiency of 55.57 % (Fig. 3a). The large irreversible capacity loss caused electrolytic decomposition, which is common in carbon materials [41]. A sloping plateau was observed at approximately 0.9 V in the first cycle, which can be attributed to the SEI film formation; this agrees well with the CV results [41]. The Charge/Discharge curves of NSC show a non-linear sloping voltage profile, indicating that the capacity contribution is mainly owing to Na-ion storage in the disordered graphene layers. Na-ion storage involves adsorption and desorption at planar surfaces, pseudo-capacitive storage on the edge and defect sites of the heteroatom dopants, and Na^+ intercalation in the graphene interlayer, as well as the surface contribution and influence of crystallinity. This is unlike the voltage profile obtained from a hard carbon anode, wherein a low-potential flat plateau appears [61]. The absence of the low-potential plateau in the voltage profile obtained from NSC reduces any risks due to Na metal plating and stripping; therefore waste-derived carbon anodes are suitable for long-term usage [62]. A long-term cycling test was also conducted on the CC and NSC electrodes at 500 mA g^{-1} . Figs. S11b and Fig. 3b show the cycling performances of the CC and NSC electrodes at a current density of 500 mA g^{-1} . The NSC electrode displays outstanding cycling stability and an extraordinary reversible capacity of

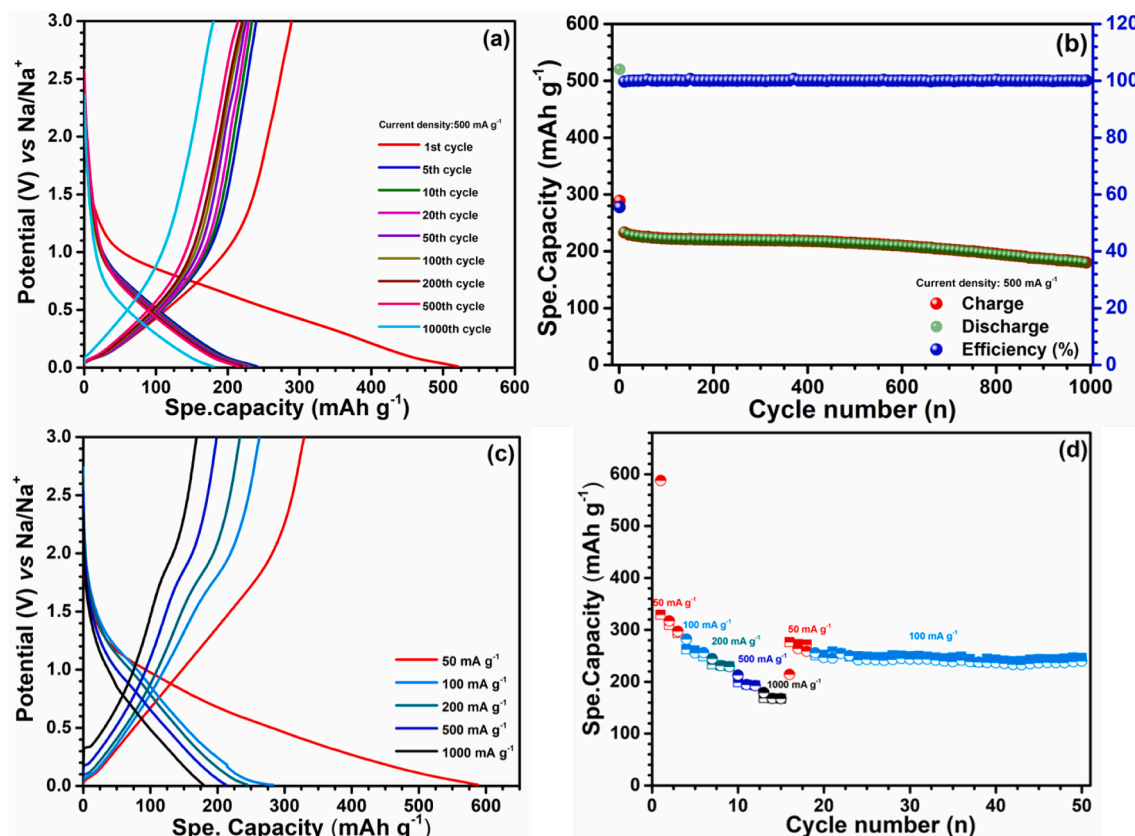


Fig. 3. Charge/discharge curves and cycle life (a and b) at a current density of 500 mA g^{-1} and (c and d) rate capability curve of the NSC//Na cell.

180 mAh g^{-1} after 1000 cycles. By contrast, the CC electrode preserves a reduced reversible capacity of 80 mAh g^{-1} , indicating that N and S co-doping can successfully improve the capacity of the NSC anode. The improved cycle stability of the NSC anode indicates that a large inter-layer spacing is beneficial for Na-ion storage at low voltages, thereby confirming the stability of the electrode material [40].

Fig. S11c and Fig. 3c display the rate capabilities of the CC and NSC electrodes, with the latter exhibiting exceptional performance. Fig. S11c displays the rate capability curve of the CC anode calculated at different current densities. Specific discharge capacities of 478, 186, 155, 120, and 92 mAh g^{-1} were obtained from the CC electrode at current densities of 50, 100, 200, 500, and 1000 mA g^{-1} , respectively. At the same current densities, specific discharge capacities obtained from NSC were 588, 282, 245, 213, and 179 mAh g^{-1} (Fig. 3c). When the current density returned to 50 mA g^{-1} , the capacities recovered to 214 mAh g^{-1} , representing the superb rate capability of NSC (Fig. 3d). These outcomes confirm that the favorable transport properties of NSC yield superior electrochemical performance. Figs. S12 display the selected charge/discharge curve and cycle life of the NSC electrodes, with 20 mg mass loadings. Initially Li//CSN and Na//CSN showed initial 1st cycle capacity of 1206, 328 mAh/g and 10th cycle capacity of 328 and 48 mAh/g . Furthermore, (Fig. S13) presents the selected charge/discharge curves and the cycle life of the NSC//NaCrO₂ cell. The charge and discharge capacities of the full cell were measured at $122.35 \text{ mAh g}^{-1}$ and 117.5 mAh g^{-1} (1C rate) then, it was tested for up to 100 cycles. The charge/discharge profiles confirmed the intercalation and deintercalation of sodium ions into the NaCrO₂ cathode.

Display the selected charge/discharge curve and cycle life of the NSC//NaCrO₂ cell. The charge and discharge capacity of the full cell is $122.35 \text{ mAh g}^{-1}$, 117.5 mAh g^{-1} respectively. The charge and discharge curves confirmed the sodium ion intercalated and de-intercalated into the NaCrO₂ cathode. The full cell was tested up to 100 cycles. The Na-ion binding ability with porous carbon is thermodynamically unfavorable

without heteroatoms, and N and S doping in carbon frameworks is an effective strategy to enhance Na-ion binding to increase capacity. The superior Na-ion diffusion kinetics at the surface of NSC is favorable for accelerating reaction kinetics.

Figs. 4 and 5 display the CV curves that were obtained under scan rates in the range of $0.2\text{--}1 \text{ mV s}^{-1}$ within a potential window of $0.01\text{--}3 \text{ V}$ vs Li/Li⁺ and Na/Na⁺ for investigating the Li- and Na-ion storage kinetics of the NSC electrode. The ion storage mechanisms can be determined based on the power-law relation using peak current (i) and scan rate (ν) [63,64].

$$i(\nu) = a\nu^b, \text{ where } a \text{ and } b \text{ are constants.}$$

The $\log(i)$ versus $\log(\nu)$ graph and its slope can be used to determine the b value. When $b = 0.5$, the diffusion-controlled process occurs, and $b = 1$ represents the surface-capacitive-contribution [63]. From Fig. 5b, the measured b values of Na-NSC are 0.9, 0.87, and 0.64 corresponding to the anodic and cathodic peaks, respectively, indicating that Na-ion storage is combined with diffusion-controlled and surface-capacitive behaviors. The Li-NSC exhibited a similar storage mechanism, and the equivalent b values were 0.87, 0.9, and 0.63 (Fig. 4b).

The following equations were used to calculate the capacitive contribution of the NSC electrode: [63,65]

$$i(\nu) = K_1\nu + K_2\nu^{1/2} \quad (1)$$

$$ori(\nu)/\nu^{1/2} = K_1\nu^{1/2} + K_2 \quad (2)$$

where i is the responsive current at different scan rates (ν) at a randomly selected potential (V) and K_1 and K_2 are constants, which can be derived from the slope and intercept of the linear relationship between $i(\nu)/\nu^{1/2}$ and $\nu^{1/2}$ at each fixed potential. The capacity contribution percentages can be calculated from the surface-controlled (capacitive contribution) and diffusion-controlled capacitances [63,65]. Fig. 5c reveals that when the scan rate increases, the capacitive contribution increases and

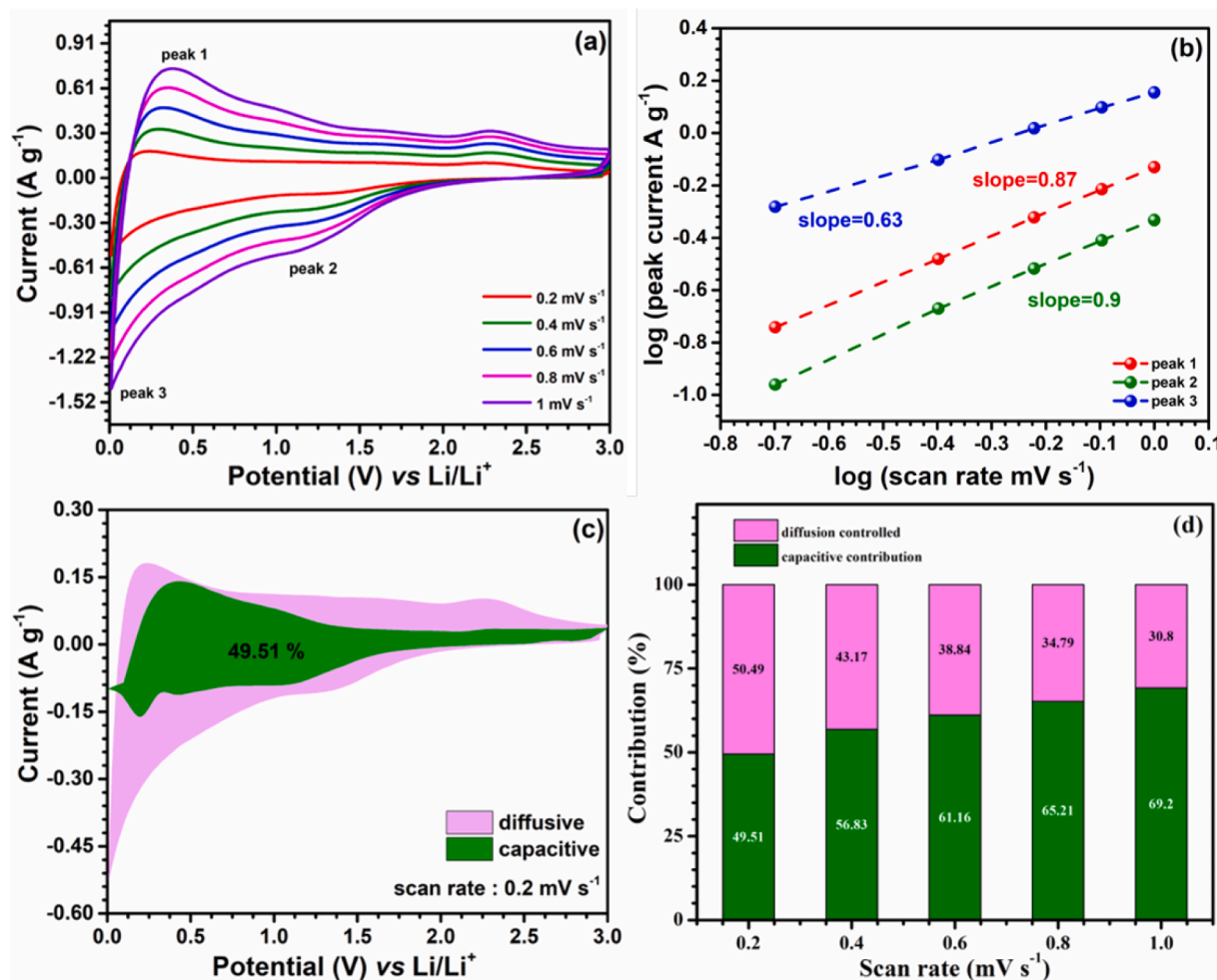


Fig. 4. Cyclic voltammetry curves of the NSC-anode-based Li cell. (a) Cyclic voltammetry curves at different scan rates (0.2–1 mV/s) and (b) log (scan rate mV/s) vs log (peak current A g⁻¹). The green CV curve represents the capacitive contribution at different scan rates: (c) 0.2, (d) 0.4, (e) 0.6, (f) 0.8, and (g) 1 mV/s. (h) Bar chart of the surface-controlled capacitances (capacitive contribution) and diffusion-controlled capacitances at corresponding scan rates.

reaches 22.46 % at a scan rate of 0.1 mV s⁻¹. The figure reveals that the capacitive contribution denoted by the green color and the diffusion-controlled current denoted by the pink color constitute the total current.

When the scan rate increased to 1 mV s⁻¹, the capacitive contribution reached its maximum of 31.38 %. In addition, the calculated pseudocapacitive contributions were 22.46 %, 25.78 %, 27.73 %, 29.57 %, and 31.38 % for Na-NSC and 49.51 %, 56.83 %, 61.16 %, 65.21 % and 69.2 % for Li-NSC at 0.2, 0.4, 0.6, 0.8, and 1 mV s⁻¹, respectively (Fig. 4h and Fig. 5h). For comparison, we conduct CV to determine the charge-storage mechanisms of the Li-CC and Na-CC cells, and the results are shown in Figs. S14 and S15. The results indicate that Li ions are easily adsorbed in the macro-micropores and defects, thereby accelerating the kinetics. The results also reveal that the Na ions are moderately adsorbed in the macro-micropores and defects, unlike the Li ions kinetic behavior. The increased ratio of pseudo capacitance is essential for facile charge transfer. To further improve the pseudocapacitive nature, an effective surface engineering technique is required to attain excellent rate capabilities in carbon-based anode materials.

Electrochemical performance of the CC and NSC anode-based LIBs and SIBs

Electrochemical impedance spectroscopy

EIS was conducted to better understand the electrochemical performances of the CC and NSC electrodes. Figs. S16a and b show the Nyquist plots, which include a high- to medium-frequency semi-circle,

of the CC and NSC electrodes. The diameter of the semi-circular loops is related to the charge-transfer resistance (R_{ct}), and an inclined line in the low-frequency region signifies the Warburg impedance [41]. The fitted circuit diagram obtained from the Nyquist plots is presented in Fig. S16. Table S1 list the electrolyte resistance (R_{ele}), solid-electrolyte interphase resistance (R_{SEI}), and charge-transfer resistance (R_{ct}) of the LIBs and SIBs constructed using the CC and NSC anode materials. The calculated R_{ct} value of Na-NSC was 31 Ω , which was lower than that of CC (42.47 Ω) owing to improved electronic conductivity and electrochemical activity resulting from N and S doping. Further, the analyzed charge-transfer resistance of Li-NSC was 61.65 Ω , which is smaller than that of CC (78.29 Ω). The solution and charge-storage resistances were considerably reduced after the incorporation of N and S heteroatoms, indicating an improved electrode–electrolyte interface that accelerated ion-transfer kinetics. After 1000 cycles, the R_{ele} , R_{SEI} , and R_{ct} values of Li-NSC and Na-NSC considerably increased (Fig. S16c and d).

Pyridinic and pyrrolic N heteroatoms in porous carbon strongly favors rapid ion-transport kinetics inside the porous architecture, and S heteroatoms vastly improve space utilization by promoting the electro-sorption of Li and Na ions. The presence of dual heteroatoms increases the polarity of the carbon pores, facilitating easy contact between the pore and electrolyte, and reducing the interface resistance to overcome the ion-diffusion losses at high current rates. Porous carbon can easily store ions in its innermost pores even at high current densities, exhibiting a high discharge capacity. Overall, From the environmental sustainability aspect the environmental waste derived carbon provided the

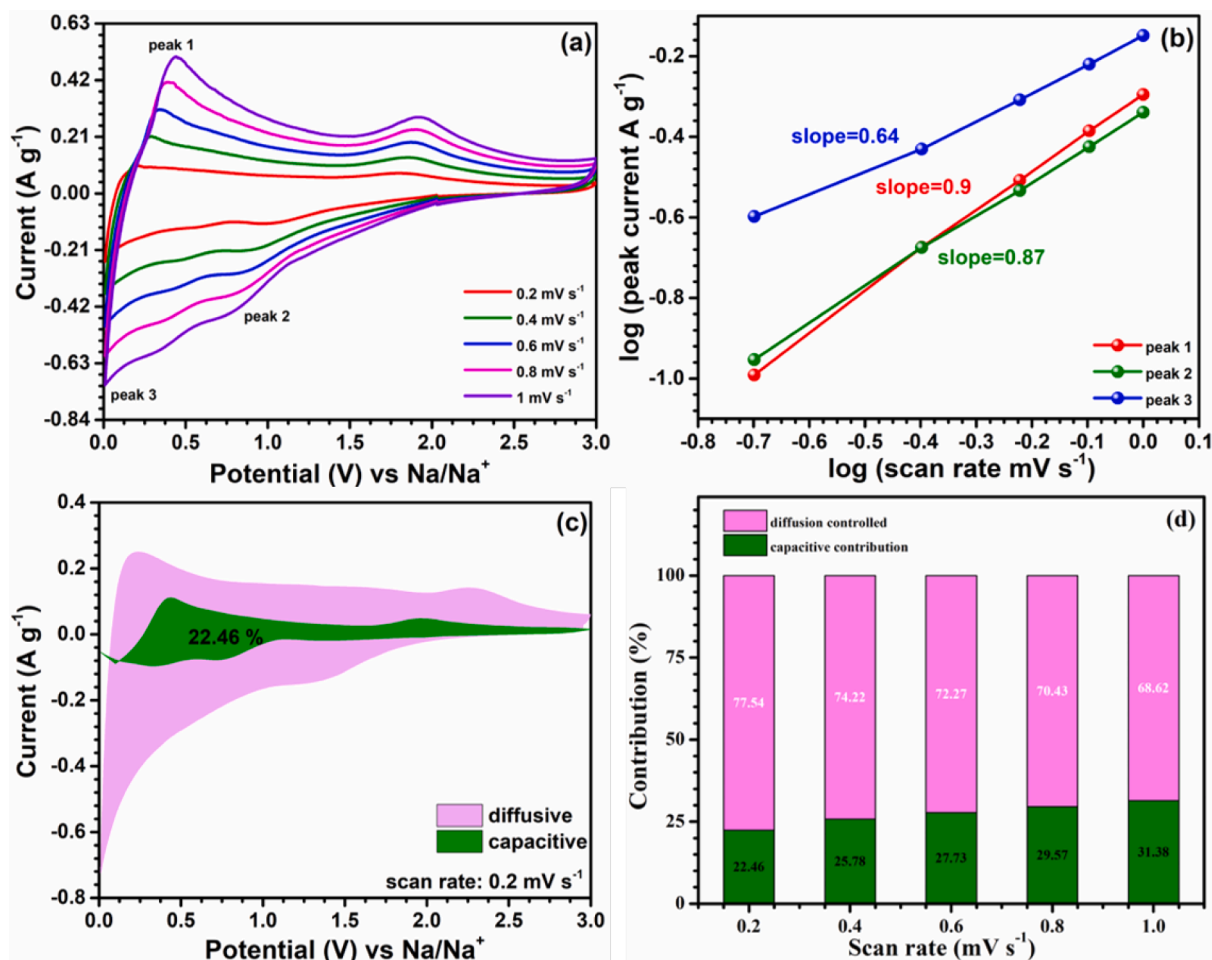


Fig. 5. Cyclic voltammetry curves of the NSC-anode-based Na cell. (a) Cyclic voltammetry curves at different scan rates (0.1–1 mV/s) and (b) log (scan rate mV/s) vs log (peak current A g⁻¹). The green-colored CV curves represent the capacitive contribution at different scan rates: (c) 0.2, (d) 0.4, (e) 0.6, (f) 0.8, and (g) 1 mV/s. (h) Bar chart of the surface-controlled capacitances (capacitive contribution) and diffusion-controlled capacitances at corresponding scan rates.

excellent electrochemical performance.

Conclusion

We successfully developed and implemented a high-performance waste-derived porous carbon anode developed via a sustainable approach for applications in LIBs and SIBs. A green chemical-activation technique using melamine as an activation agent and cigarette butts as a waste resource can yield porous carbon with high surface area and pore volume with major pore sizes between 2.44–10.7 nm. This porous carbon can effectively act as a high-capacity anode for applications in high-energy-density LIBs and SIBs. Notably, porous carbon can effectively cycle for more than 1000 cycles with a retention of 62 % and a good capacity at a high current rate of 1000 mA g⁻¹, outperforming conventional graphite and hard carbon anodes. Further study on optimizes the N and S doping concentration and increasing the surface area of the carbon framework will be carried out in future. This study provides new opportunities for processing environmental waste through a sustainable method to synthesize a high-performing anode material, which applies to future energy storage devices.

CRediT authorship contribution statement

Ramkumar Balasubramaniam: Methodology, Investigation, Formal analysis, Data curation, Conceptualization. **Ranjith Thangavel:** Investigation, Formal analysis, Data curation. **Hariharan**

Dhanasekaran: Conceptualization, Data curation, Formal analysis. **Megala Moorthy:** Conceptualization, Data curation, Formal analysis. **Sangho Park:** Formal analysis, Data curation, Conceptualization. **Werayut Srituravanich:** Methodology, Formal analysis, Data curation. **Hyun-Yong Lee:** Methodology, Formal analysis, Data curation. **Yun-Sung Lee:** Validation, Supervision, Resources, Project administration, Investigation, Funding acquisition, Formal analysis, Data curation, Conceptualization.

Declaration of competing interest

The authors declare that they have no known competing financial interests or personal relationships that could have appeared to influence the work reported in this paper.

Acknowledgement

This research was financially supported by a National Research Foundation of Korea, South Korea (NRF) grant funded by the Korean government (Ministry of Science, ICT & Future Planning) (No. RS-2023-00208361).

Appendix A. Supplementary material

Supplementary data to this article can be found online at <https://doi.org/10.1016/j.jiec.2024.12.036>.

References

- [1] K. Yu, J. Li, H. Qi, C. Liang, High-capacity activated carbon anode material for lithium-ion batteries prepared from rice husk by a facile method, *Diam. Relat. Mater.* 86 (2018) 139–145.
- [2] B. Ramkumar, K. So-young, N. Chan-woo, V. Aravindan, L. Yun-Sung, LiBO_2 -modified LiCoO_2 as an efficient cathode with garnet framework $\text{Li}_{6.75}\text{La}_3\text{Zr}_{1.75}\text{Nb}_{0.25}\text{O}_{12}$ electrolyte toward building all-solid-state lithium battery for high-temperature operation, *Electrochim. Acta.* 359 (2020) 136955.
- [3] B. Ramkumar, C. Nam, V. Aravindan, D. Eum, K. Kang, Y.S. Lee, Interfacial engineering in a cathode composite based on garnet-type solid-state Li-ion battery with high voltage cycling, *ChemElectroChem.* 8 (2021) 570–576.
- [4] J.C. Seol, B. Ramkumar, V. Aravindan, R. Thangavel, Y.S. Lee, Ameliorating the electrode/electrolyte interface compatibility in Li-ion solid-state batteries with plasticizer, *J. Alloy. Compd.* 927 (2022) 167077.
- [5] B. Ramkumar, V. Aravindan, H. Ramasamy, K.V. Ajeya, J.G. Ryu, H.Y. Jung, Y. S. Lee, Ternary metal oxide filled PEO-based polymer electrolyte for solid-state lithium metal battery: The role of filler particle size, *Solid State Sci.* 132 (2022) 106958.
- [6] B. Ramkumar, S. Yuvaraj, S. Surendran, K. Pandi, H.V. Ramasamy, Y.S. Lee, R. K. Selvan, Synthesis and characterization of carbon coated $\text{LiCo}_{1/3}\text{Ni}_{1/3}\text{Mn}_{1/3}\text{O}_2$ and bio-mass derived graphene like porous carbon electrodes for aqueous Li-ion hybrid supercapacitor, *J. Phys. Chem. Solid.* 112 (2018) 270–279.
- [7] B. Ramkumar, C.W. Nam, V. Aravindan, J.C. Seol, K.V. Ajeya, H.Y. Jung, Y.S. Lee, Composite solid electrolyte for high voltage solid-state Li-metal battery, *ChemElectroChem.* 9 (2022) e202200317.
- [8] S. Akhtar, W. Lee, M. Kim, M.S. Park, W.S. Yoon, Conduction mechanism of charge carriers in electrodes and design factors for the improvement of charge conduction in Li-ion batteries, *J. Electrochem. Sci. Technol.* 12 (2021) 1–20.
- [9] S.B. Lee, B. Ramkumar, Double-shelled hybrid $\text{MgFe}_2\text{O}_4/\text{Fe}_2\text{O}_3$ hollow microspheres as a high-capacity anode for lithium-ion batteries, *J. Ind. Eng. Chem.* 110 (2022) 262–273.
- [10] P. Zeng, C. Zhang, M. Ding, Y. Huang, A simple fabrication of porous carbon@tin dioxide as anode material for achieving lithium-ion batteries with high performance, *Carbon Lett.* 33 (2023) 1699–1705.
- [11] Y. Wen, X. Wang, J. Huang, Y. Li, T. Li, B. Ren, Coffee grounds derived sulfur and nitrogen dual-doped porous carbon for the cathode material of lithium-sulfur batteries, *Carbon Lett.* 33 (2023) 1265–1278.
- [12] J.H. Kim, S. Kim, J.H. Han, S.B. Seo, Y.R. Choi, J. Lim, Y.A. Kim, Perspective on carbon nanotubes as conducting agent in lithium-ion batteries: the status and future challenges, *Carbon Lett.* 33 (2023) 325–333.
- [13] N. Ha, S.G. Jeong, C. Lim, S. Ha, C.G. Min, Y. Choi, Y.S. Lee, Preparation and electrochemical characteristics of waste-tire char-based CFX for lithium-ion primary batteries, *Carbon Lett.* 33 (2023) 1013–1018.
- [14] D. Han, G. Yu, A. Liu, G. Li, W. Wang, B. He, Z. Hou, H. Yin, Soft-template-assisted synthesis of N-doping layered Co_2S_3 nanoparticles as an advanced anode for sodium-ion batteries, *Carbon Lett.* 33 (2023) 1839–1846.
- [15] Y. Shen, L. Wang, J. Jiang, D. Wang, D. Zhang, D. Yin, L. Wang, X. Zhang, G. Huang, Y. Cheng, Stabilization of high-voltage layered oxide cathode by multi-electron rare earth oxide, *Chem. Eng. J.* 454 (2023) 140249.
- [16] C. Zhang, F. Wang, J. Han, S. Bai, J. Tan, J. Liu, F. Li, Challenges and recent progress on silicon-based anode materials for next-generation lithium-ion batteries, *Small Struct.* 2 (2021) 2100009.
- [17] W. Qi, J.G. Shapter, Q. Wu, T. Yin, G. Gao, D. Cui, Nanostructured anode materials for lithium-ion batteries: Principle, recent progress and future perspectives, *J. Mater. Chem. A* 5 (2017) 19521–19540.
- [18] X. Zuo, J. Zhu, P. Müller-Buschbaum, Y.J. Cheng, Silicon based lithium-ion battery anodes: a chronicle perspective review, *Nano Energy* 31 (2017) 113–143.
- [19] Q. Jiang, Z. Zhang, S. Yin, Z. Guo, S. Wang, C. Feng, Biomass carbon micro/nano-structures derived from ramie fibers and corncobs as anode materials for lithium-ion and sodium-ion batteries, *Appl. Surf. Sci.* 379 (2016) 73–82.
- [20] H. Kim, D.I. Kim, W.S. Yoon, Challenges and design strategies for conversion-based anode materials for lithium-and sodium-ion batteries, *J. Electrochem. Sci. Technol.* 13 (2022) 32–53.
- [21] L. Qie, W. Chen, X. Xiong, C. Hu, F. Zou, P. Hu, Y. Huang, Sulfur-doped carbon with enlarged interlayer distance as a high-performance anode material for sodium-ion batteries, *Adv. Sci.* 2 (2015) 1500195.
- [22] R.R. Gaddam, D. Yang, R. Narayan, K.V.S.N. Raju, N.A. Kumar, X.S. Zhao, Biomass derived carbon nanoparticle as anodes for high performance sodium and lithium ion batteries, *Nano Energy* 26 (2016) 346–352.
- [23] M. Inaba, Secondary Batteries - lithium rechargeable systems - lithium-ion negative electrodes: graphite, *Encycl. Electrochem. Power Sources*. (2009) 198–208.
- [24] G. Zheng, J. Yin, Z. Guo, S. Tian, X. Yang, Embedding cobalt into ZIF-67 to obtain cobalt-nanoporous carbon composites as electrode materials for lithium ion battery, *J. Electrochem. Sci. Technol.* 12 (2021) 458–464.
- [25] H. Kim, D.I. Kim, W.S. Yoon, Enhancing electrochemical performance of $\text{Co}(\text{OH})_2$ anode materials by introducing graphene for next-generation Li-ion batteries, *J. Electrochem. Sci. Technol.* 13 (2022) 398–406.
- [26] S. Yuvaraj, M.S. Park, V.G. Kumar, Y.S. Lee, D.W. Kim, Electrochemical performance of M_2GeO_4 ($\text{M} = \text{Co}, \text{Fe}$ and Ni) as anode materials with high capacity for lithium-ion batteries, *J. Electrochem. Sci. Technol.* 8 (2017) 323–330.
- [27] R. Thangavel, A.S. Pandian, H.V. Ramasamy, Y.S. Lee, Rapidly synthesized, few-layered pseudocapacitive SnS_2 anode for high-power sodium ion batteries, *ACS Appl. Mater. Interf.* 9 (2017) 40187–40196.
- [28] Q. Jin, W. Li, K. Wang K, P. Feng, H. Li, T. Gu, M. Zhou, W. Wang, S. Cheng, K. Jiang. Experimental design and theoretical calculation for sulfur-doped carbon nano fibers as a high. 7 (2019) 10239–10245.
- [29] K. Kim, R.A. Adams, P.J. Kim, A. Arora, E. Martinez, J.P. Youngblood, V.G. Pol, Li-ion storage in an amorphous, solid, spheroidal carbon anode produced by dry-autoclaving of coffee oil, *Carbon N Y.* 133 (2018) 62–68.
- [30] A. Singh, D.K. Kohli, R. Singh, S. Bhartiya, M.K. Singh, A.K. Karnal, Incorporation of graphitic porous carbon for synthesis of composite carbon aerogel with enhanced electrochemical performance, *J. Electrochem. Sci. Technol.* 12 (2021) 204–211.
- [31] G. Gao, L.Z. Cheong, D. Wang, C. Shen, Pyrolytic carbon derived from spent coffee grounds as anode for sodium-ion batteries, *Carbon Resour. Convers.* 1 (2018) 104–108.
- [32] S.Y. Tsai, R. Muruganantham, S.H. Tai, B.K. Chang, S.C. Wu, Y.L. Chueh, W.R. Liu, Coffee grounds-derived carbon as high performance anode materials for energy storage applications, *J. Taiwan Inst. Chem. Eng.* 97 (2019) 178–188.
- [33] C. Yu, H. Hou, X. Liu, L. Han, Y. Yao, Z. Dai, D. Li, The recovery of the waste cigarette butts for N-doped carbon anode in lithium ion battery, *Front. Mater.* 5 (2018) 63.
- [34] T.S. Blankenship, R. Mokaya, Cigarette butt-derived carbons have ultra-high surface area and unprecedented hydrogen storage capacity, *Energ. Environ. Sci.* 10 (2017) 2552–2562.
- [35] M. Sevilla, N. Diez, A.B. Fuertes, More sustainable chemical activation strategies for the production of porous carbons, *ChemSusChem.* 14 (2021) 94–117.
- [36] E.A. Smith, T.E. Novotny, Whose butt is it? Tobacco industry research about smokers and cigarette butt waste, *Tob. Control.* 20 (2011) i2–i8.
- [37] R. Li, A. Cao, Y. Zhang, G. Li, F. Jiang, S. Li, D. Chen, C. Wang, J. Ge, C. Shu, Formation of nitrogen-doped mesoporous graphitic carbon with the help of melamine, *ACS Appl. Mater. Interf.* 6 (2014) 20574–20578.
- [38] H. Tang, D. Yan, T. Lu, L. Pan, *Electrochimica Acta* Sulfur-doped carbon spheres with hierarchical micro / mesopores as anode materials for sodium-ion batteries, *Electrochim. Acta.* 241 (2017) 63–72.
- [39] L. He, Y.R. Sun, C.L. Wang, High performance sulphur-doped pitch-based carbon materials as anode materials for sodium-ion batteries, *New Carbon Mater.* 35 (2020) 420–427.
- [40] W. Song, J. Kan, H. Wang, X. Zhao, Y. Zheng, H. Zhang, L. Tao, M. Huang, W. Liu, J. Shi, Nitrogen and sulfur Co-doped mesoporous carbon for sodium ion batteries, *ACS Appl. Nano Mater.* 2 (2019) 5643–5654.
- [41] L. Wang, L. Hu, W. Yang, D. Liang, L. Liu, S. Liang, C. Yang, Z. Fang, Q. Dong, C. Deng, N/S-Co-Doped Porous Carbon Sheets Derived from Bagasse as High-Performance Anode Materials for Sodium-Ion Batteries. 9 (2019) 1203.
- [42] Y. Li, B. Ni, X. Li, X. Wang, D. Zhang, Q. Zhao, J. Li, T. Lu, W. Mai, L. Pan, High performance Na-ion storage of s-doped porous carbon derived from conjugated microporous polymers, *Nano-Micro Lett.* 11 (2019) 60.
- [43] D. Wu, F. Sun, Z. Qu, H. Wang, Z. Lou, B. Wu, G. Zhao, Multi-scale structure optimization of boron-doped hard carbon nanospheres boosting the plateau capacity for high performance sodium ion batteries, *J. Mater. Chem. A* 10 (2022) 17225–17236.
- [44] T. Jiang, Y. Wang, K. Wang, Y. Liang, D. Wu, P. Tsiakaras, S. Song, A novel sulfur-nitrogen dual doped ordered mesoporous carbon electrocatalyst for efficient oxygen reduction reaction, *Appl. Catal. B Environ.* 189 (2016) 1–11.
- [45] R. Li, F. Liu, Y. Zhang, M. Guo, D. Liu, Nitrogen, sulfur Co-Doped hierarchically porous carbon as a metal-free electrocatalyst for oxygen reduction and carbon dioxide reduction reaction, *ACS Appl. Mater. Interf.* 12 (2020) 44578–44587.
- [46] H. Tang, D. Yan, T. Lu, L. Pan, Sulfur-doped carbon spheres with hierarchical micro/mesopores as anode materials for sodium-ion batteries, *Electrochim. Acta.* 241 (2017) 63–72.
- [47] Y. Lu, K.H. Shin, Y. Yu, Y. Hu, J. Liang, K. Chen, H. Yuan, H.S. Park, D. Wang, Multiple active sites carbonaceous anodes for Na^+ storage: synthesis, electrochemical properties and reaction mechanism analysis, *Adv. Funct. Mater.* 31 (2021) 2007247.
- [48] J. Liang, Z. Wang, L. Huang, P. Zou, X. Liu, Q. Ni, X. Wang, W. Wang, R. Tao, Facile and tunable synthesis of nitrogen-doped graphene with different microstructures for high-performance supercapacitors, *ACS Mater. Lett.* 5 (2023) 944–954.
- [49] J. Zhang, H. Yang, Z. Huang, H. Zhang, X. Lu, J. Yan, K. Cen, Z. Bo, Pore-structure regulation and heteroatom doping of activated carbon for supercapacitors with excellent rate performance and power density. 5 (2023) 417–426.
- [50] Y. Li, B. Ni, X. Li, X. Wang, D. Zhang, Q. Zhao, J. Li, T. Lu, W. Mai, L. Pan, High-Performance Na-ion storage of S-doped porous carbon derived from conjugated microporous polymers, *Nano-Micro Lett.* 11 (2019) 60.
- [51] S. Chen, R. Tao, J. Tu, P. Guo, G. Yang, W. Wang, J. Liang, S.Y. Lu, High performance flexible lithium-ion battery electrodes: ion exchange assisted fabrication of carbon coated nickel oxide nanosheet arrays on carbon cloth, *Adv. Funct. Mater.* 31 (2021) 2101199.
- [52] K. Du, R. Tao, C. Guo, H. Li, X. Liu, P. Guo, D. Wang, J. Liang, J. Li, S. Dai, X.G. Sun, In-situ synthesis of porous metal fluoride@carbon composite via simultaneous etching/fluorination enabled superior Li storage performance, *Nano Energy* 103 (2022) 107862.
- [53] K.R. Saravanan, N. Kalaiselvi, Nitrogen containing bio-carbon as a potential anode for lithium batteries, *Carbon* 81 (2015) 43–53.
- [54] P. Han, Y. Yue, L. Zhang, H. Xu, Z. Liu, K. Zhang, C. Zhang, S. Dong, W. Ma, G. Cui, Nitrogen-doping of chemically reduced mesocarbon microbead oxide for the improved performance of lithium ion batteries, *Carbon* 50 (2012) 1355–1362.
- [55] H. Zhang, W. Zhou, D. Huang, L. Ou, Z. Lan, X. Liang, H. Huang, D. Huang, J. Guo, Functionalized hierarchical porous carbon with sulfur/nitrogen/oxygen tri-doped

- as high quality sulfur hosts for lithium-sulfur batteries, *J. Alloy. Compd.* 858 (2021) 157647.
- [56] A. Vesel, R. Zaplotnik, G. Primc, M. Mozetič, A review of strategies for the synthesis of n-doped graphene-like materials, *Nanomaterials*. 10 (2020) 2286.
- [57] L. Fu, K. Tang, K. Song, P.A. Van Aken, Y. Yu, J. Maier, Nitrogen doped porous carbon fibres as anode materials for sodium ion batteries with excellent rate performance, *Nanoscale*. 6 (2014) 1384–1389.
- [58] L. Xia, Z. Song, L. Zhou, D. Lin, Q. Zheng, Nitrogen and oxygen dual-doped hierarchical porous carbon derived from rapeseed meal for high performance lithium-sulfur batteries, *J. Solid State Chem.* 270 (2019) 500–508.
- [59] K. Tang, L. Fu, R.J. White, L. Yu, M.M. Titirici, M. Antonietti, J. Maier, Hollow carbon nanospheres with superior rate capability for sodium-based batteries, *Adv. Energy Mater.* 2 (2012) 873–877.
- [60] Y. Wen, K. He, Y. Zhu, F. Han, Y. Xu, I. Matsuda, Y. Ishii, J. Cumings, C. Wang, Expanded graphite as superior anode for sodium-ion batteries, *Nat. Commun.* 5 (2014) 4033.
- [61] B. Babu, P. Simon, A. Balducci, Fast charging materials for high power applications, *Adv. Energy Mater.* 10 (2020) 2001128.
- [62] R. Thangavel, A.G. Kannan, R. Ponraj, G. Yoon, V. Aravindan, D.W. Kim, K. Kang, W.S. Yoon, Y.S. Lee, Surface enriched graphene hollow spheres towards building ultra-high power sodium-ion capacitor with long durability, *Energy Storage Mater.* 25 (2020) 702–713.
- [63] B. Cheng, X. Li, L. Pan, H. Xu, H. Duan, Q. Wu, B. Yin, H. He, Ultra-thin wrinkled carbon sheet as an anode material of high-power-density potassium-ion batteries, *Molecules*. 27 (2022) 2973.
- [64] Q. Jin, K. Wang, P. Feng, Z. Zhang, S. Cheng, K. Jiang, Surface-dominated storage of heteroatoms-doping hard carbon for sodium-ion batteries, *Energy Storage Mater.* 27 (2020) 43–50.
- [65] K. Xu, Y. Li, J. Xiong, X. Ou, W. Su, G. Zhong, C. Yang, Activated amorphous carbon with high-porosity derived from camellia pollen grains as anode materials for lithium/sodium ion batteries, *Front. Chem.* 6 (2018) 366.